2.5 MICROSTRUCTURAL SUMMARY OF ODS FERRITIC ALLOYS (14YW, 14YWT, 12YWT, MA957FR, PM2000) AND RAFM STEELS (F82H MOD.3-CW, EUROFER97) FROM JP27 IN-SITU HE INJECTION (ISHI) EXPERIMENT AT 500°C —

H. J. Jung, D. J. Edwards, R. J. Kurtz (Pacific Northwest National Laboratory), G. R. Odette, Y. Wu, T. Yamamoto (University of California Santa Barbara)

OBJECTIVE

To summarize the microstructural response of oxide dispersion strengthened (ODS) ferritic alloys (14YW, 14YWT, 12YWT, MA957Fr, PM2000) and reduced activation ferritic/martensitic (RAFM) steels (F82H mod.3-CW, Eurofer97) irradiated in the JP27 irradiation experiment in HFIR at 500°C with *in situ* He injection (ISHI).

SUMMARY

A TEM characterization of various ferritic-based alloys has been conducted to document the changes in microstructure under neutron irradiation with and without the impact of high levels of He injection. Microstructural features such as dislocation loops, network dislocations, He bubbles and voids were characterized in five ODS alloys, 14YW, 14YWT, 12YWT, MA957Fr, PM2000, and two RAFM steels, F82H mod.3+CW and Eurofer97. The total neutron dose was ~21.2 dpa and the total He level was ~1230 appm injected into an ~6 µm uniform region below the surface of the sample. The results indicated that He injection significantly impacts the microstructure evolution path, producing changes in the dislocation structure and cavity distribution that are closely related to the size, density and chemistry of the oxide particles, or the lack thereof in the case of the RAFM alloys.

PROGRESS AND STATUS

Introduction

Oxide-dispersed strengthened (ODS) ferritic alloys, nanostructured ferritic alloys (NFA) and reduced activation ferritic/martensitic (RAFM) steels are generally swelling-resistant under neutron irradiation [1,2]. However, the swelling resistance of RAFM steels could degrade in the presence of high levels of helium (10 appm He per dpa) produced by transmutation in the fusion nuclear environment [3]. Over the lifetime of the first wall, up to ~2000 appm of helium will accumulate in these materials, leading to helium bubble formation, hardening of the matrix, and possibly loss of creep-rupture strength at high irradiation temperatures. A potential consequence of helium accumulation is that small bubbles (d<2 nm) can grow to a critical size and convert to unstably growing voids, thereby causing significant swelling [4]. In order to prevent the transition of He bubbles to voids, microstructures are being designed to provide a high density of nanoscale trapping sites such as nano-size oxide particles to broadly disperse He gas atoms [1] so that bubbles do not reach the critical size. We are currently examining the effectiveness of oxide dispersions, as well as elucidating the mechanisms of He movement, trapping, and interaction with various defects and interfaces in ODS ferritic alloys and RAFM steels under irradiation.

Due to practical difficulties in exploring material performance in a fusion-relevant irradiation environment, the *in situ* He injection (IHSI) technique has been developed to explore the effects of simultaneous neutron irradiation and He injection on microstructural evolution of candidate materials, as detailed in the recent literature [5-9]. Here we present analytical transmission electron microscopy (TEM) characterization of neutron-irradiated and He/neutron-irradiated effects on ODS ferritic alloys, nanostructured ferritic alloys and RAFM steels with a NiAl layer deposited on one surface. When irradiated with neutrons, the ^{59}Ni isotope undergoes a ^{59}Ni(n, α) reaction and injects some fraction of the energetic He into the ferritic alloy. Cross-sectional TEM samples were prepared to characterize microstructural features such as He bubbles/voids, dislocation loops/line dislocations, and oxide or carbide particles.

Experimental Procedure

Three NFAs, 14YWT, 12YWT, MA957Fr, two ODS ferritic alloys 14YW and PM2000, and two RAFM steels (F82H mod.3-CW, Eurofer97) were neutron irradiated in the JP27 experiment to a dose of 21.2 dpa at 500°C in the High Flux Isotope Reactor (HFIR) at Oak Ridge National Laboratory (ORNL). A list of the various alloys and their nominal compositions in the as-irradiated state as determined by energy dispersive spectroscopy (EDS) is provided in Table 1. Note that the alloys containing W have experienced some degree of transmutation in the highly thermalized neutron environment of HFIR such that some of W has converted into Os and Re. A 4 µm NiAl coating used for the ISHI was applied to one side of a 3-mm TEM disc, which allows FIB lamella to be extracted from either side of a TEM disc to explore the impact of neutron irradiation with or without concurrent helium injection. At 21.2 dpa, the NiAl coating produced a He concentration of about 1230 appm in the ferritic matrix extending to a depth of ~6 µm below the coating. Cross-sectional TEM samples, prepared by a FIB (FEI Quanta 3D), were finalized with low-energy surface cleaning (2 keV Ga^+ ion) at ±2° tilt angles. The TEM lamellae were extracted from each side of the TEM disc.

TEM characterization was performed using a JEOL 2010F and a newly installed Cs-corrected JEOL ARM 200CF microscope operated at 200 keV. Bright-field TEM/STEM images of dislocation loops and line dislocations were acquired under weak ***g***=200 two-beam conditions near 001 zone axis following the approach outlined by Yao et al [10]. This approach allows the <100>/{100} and 1/2<111>/{111} type dislocation loop populations to be measured separately at a given orientation based on loop inclination, shape of the loop, and the ***g.b=0*** invisibility criterion. Bright-field TEM (BFTEM) images of He bubbles and voids were acquired using an over/under-focus technique, and measured bubble sizes are about 87% of the actual bubble size at an under-defocus of 750 nm as determined from a previous modeling study [11-13].

Table 1. Composition of alloys

Alloy	Composition (wt.%) with Fe balance											
	Al	Si	Ti	Cr	Mn	Fe	Ni	Y	Mo	W	Re	Os
14YW	1.6	0.8	0.0	13.7	1.9	80	0.1	0.1	0.0	2.0	0.1	0.5
14YWT	0.8	0.2	0.4	13.8	2.2	79	0.1	0.1	0.1	2.0	0.2	0.5
12YWT	0.8	0.1	0.4	12.0	2.1	81	0.4	0.1	0.3	1.7	0.2	0.5
MA957Fr	0.4	0.3	---	8.9	2.4	87	0.1	---	---	0.8	---	0.2
PM2000	6.0	1.0	0.5	18.5	1.8	71	0.1	0.3	0.1	0.00	0.1	0.0
F82H.mod3 +CW	---	0.1	---	8.2	0.3	88	---	---	---	1.3	0.2	0.5
Eurofer	0.5	0.9	---	8.6	2.7	80	0.8	---	0.6	0.8	0.1	0.3

Results and Discussion

The microstructural information is provided for the He-injected/neutron irradiated side versus the neutron-irradiated side of the same sample. Figure 1 presents examples of the dislocation loops and line dislocations taken in BFTEM using a weak **g**=200 two-beam condition near a 001 zone axis. For brevity the two types of loops will be referred to as <100> or <111> loops to represent the <100>/{100} and 1/2<111>/{111} loops, respectively, documented in this work. Figure 2 provides examples of the cavity microstructure present in each irradiated material and condition; each image was taken in an underfocus/overfocused condition of 750 nm. Histograms of the loop and cavity sizes for each alloy and irradiation condition are provided in Figure 3 - Figure 5. The density and average size values are summarized in Table 2.

Table 2. Microstructure summary at 500 °C of JP27 ODS ferritic alloys and RAFM steels under irradiation of only neutron and dual He/neutron

Sample	Irradiation Condition @ 500 °C	Dislocation loops Density [$10^{20}/m^3$] (Size [nm])		Line Dislocation Density [$10^{13}/m^2$]	Cavities (He bubbles or voids)	
		<100>{100}	1/2<111>{111}		Density [$10^{22}/m^3$]	Size [nm]
14YWT	neutron	18 (11.2 ±7.1)	15 (8.9 ±6.6)	6.3	N/A	N/A
	He/neutron	36 (17.1 ±11.2)	18 (16.4 ±9.2)	5.6	19	1.4 ±0.3
12YWT	neutron	28 (6.1 ±2.8)	20 (6.9 ±3.7)	18	N/A	N/A
	He/neutron	34 (14.5 ±8.8)	28 (10.5 ±3.8)	17	19	1.2 ±0.2
MA957Fr	neutron	16 (10.1 ±4.8)	8 (13.3 ±5.0)	17	N/A	N/A
	He/neutron	30 (21.9 ±19.2)	11 (27.4 ±20.0)	27	He bubbles	
					0.4	1.9 ±0.4
					Voids in matrix	
					0.8	6.6 ±2.9
PM2000	neutron	8 (17 ±7.3)	4 (19.6 ±6.7)	22	He bubbles	
					N/A	N/A
					Voids within ODS	
					0.01	8.8 ±5.0
	He/neutron	38 (40 ±25.7)	14 (30.5 ±18)	3.7	He bubbles	
					2	1.4 ±0.2
					Voids within ODS	
					0.2	7.8 ±2.5
14YW	neutron	12 (21.7 ±15.6)	11 (17.3 ±8.9)	1.6	0.6	11.6 ±4.9
	He/neutron	27 (27.5 ±24.9)	12 (23.2 ±16.4)	2.4	11	3.1 ±1.9
F82H mod.3+CW	neutron	15 (10.3 ±5.8)	9 (10.1 ±4.9)	27	2.1	1.3 ±0.3
	He/neutron	48 (34 ±24.6)	28 (36.6 ±25.2)	30	11	2.7 ±1.6
Eurofer97	neutron	16 (9.3 ±2.7)	8 (10.2 ±4.3)	22	N/A	N/A
	He/neutron	28 (27.7 ±10.1)	11 (28.5 ±12.3)	32	He bubbles	
					0.2	1.8 (0.5)
					Voids in matrix	
					0.75	6.9 (3.6)

There are many notable differences in the response of the different materials to the presence of high helium levels. The dislocation analysis revealed that the line dislocation density and the loop densities were usually higher on the He-injected side of the sample for all of the materials. In the case of the dislocation loops, the general trend is higher dislocation loop density of both types, and a larger average diameter for both types of loops compared to the side of the sample that experienced only neutron irradiation. In addition, a consistent trend among all of the alloys is that the <100> loops are present at a higher density and larger average size compared to the <111> loops, and this trend applies equally to both sides of the sample, i.e., with and without helium injection. Perhaps the biggest surprise is the PM2000 alloy, which is a very large grained material with a relatively low density of coarse Y-Al-O particles. Large dislocation loops of both types formed during irradiation, growing to sizes of over 100 nm in the presence of helium injection. Evidently the loops were stabilized by nucleation and growth of fine helium bubbles that formed on the periphery of each <100> and <111> loop. This association between loops and helium bubbles was not observed in any of the other alloys, and is thought to have arisen in PM2000 because of the absence of a high density of grain or lath boundaries, which provide effective, competing sinks for both helium and point defects.

Under helium injection, the RAFM steels possess the lowest swelling resistance of all of the alloys due to the formation of comparatively large voids in the interiors of the martensitic laths, as well as small bubbles

on lath boundaries. These voids are often aligned in stringers that are assumed to have formed on dislocations that have migrated away under irradiation. A low density of bubbles was found in the matrix of the neutron irradiated side of the RAFM steels samples, presumably from helium produced via transmutation of the bulk alloy. At the other end of the spectrum are the two NFA 14YWT and 12YWT, which do not form any voids, only a high density of small bubbles in the helium-injected side of the TEM disc. It is assumed that helium bubbles form on the high density of nano-oxide particles (<2 nm in size) present in both alloys. MA957Fr is another NFA that exhibits mostly bubble formation, however, there were cases of void-like features that formed on particles in limited areas of the TEM foil. These may be coalescence of small bubbles on the periphery of the particles. The 14YW alloy, an analogue to 14YWT but without the titanium addition that refines the oxide particle distribution, exhibited the worst response of the NFA alloys, exhibiting both bubbles and voids that were attached to the oxide particles, as shown in Figure 6. The particles proved to be effective sinks, but their density is too low to provide the kind of sink strength that prevents helium bubbles from reaching critical size leading to unstable void growth. The oxide particles in 14YW are large enough to be easily visible in TEM, unlike those present in the 14YWT and 12YWT. It was also noted in Figure 6 that some of the bubbles and voids were aligned along the <100> planes in the 14YW alloy, perhaps because of a prior dislocation structure that no longer exists in the irradiated samples. PM2000 proved to be resistant to large-scale void formation also, but by a different mechanism. The oxide dispersion in the PM2000 consists of Y-Al-O particles with an average size of 30 nm, which amorphosized under irradiation. Their distribution is too coarse to provide the same sink strength as the nano-oxide dispersions in 14YWT and 12YWT, however, the dislocation loops that formed under irradiation proved to be effective sinks for helium, promoting a more uniform distribution of helium bubbles on the periphery of the growing loops. The only voids found in this alloy were voids that formed inside the amorphous oxide particles. Voids were found in every particle in the helium-injected side, but in only ~22% of the amorphous particles on the side of the disc without helium injection. Other microstructural changes were observed in this alloy, and have been reported in a previous semiannual report. The most notable changes are fine precipitation of a Fe-Al-Ti phase, α or possibly σ phase. It is unclear how the chemistry of this alloy affects helium transport and capture, nor its impact on the dislocation loop stability versus the lack of competing sinks because of the much larger grain size.

In summary, the NFA alloys 14YWT, 12YWT and MA957Fr are more resistant to void swelling due to trapping of helium by the high density of small nano-oxide clusters dispersed in the matrix. The PM2000 alloy also appears to be relatively resistant to void formation due to the ability of the loops to grow and continuously capture helium at the periphery of each <100> and <111> loop. The effect of the oxide particle distribution and its chemistry on helium trapping efficiency are illustrated by comparing the 14YWT versus the 14YW alloy, where the coarser distribution of particles in the 14YW allows helium bubbles to reach the critical size for unstable void growth. Since each visible particle in 14YW has a helium bubble or void associated with it, the particles appear to be effective trapping sites, but are not at a high enough density to prevent void formation. The RAFM steels are, not surprisingly, the poorest of the group of alloys investigated here with respect to void swelling in the presence of high helium.

Future work will continue to explore the microstructure of these irradiated alloys, expanding the matrix to higher doses and exploring samples irradiated at 400°C under similar helium injection levels. 3D-APT measurements are also being done on certain alloys to help understand the fate of the nano-oxide dispersion, as well as the presence of any precipitation in the matrix.

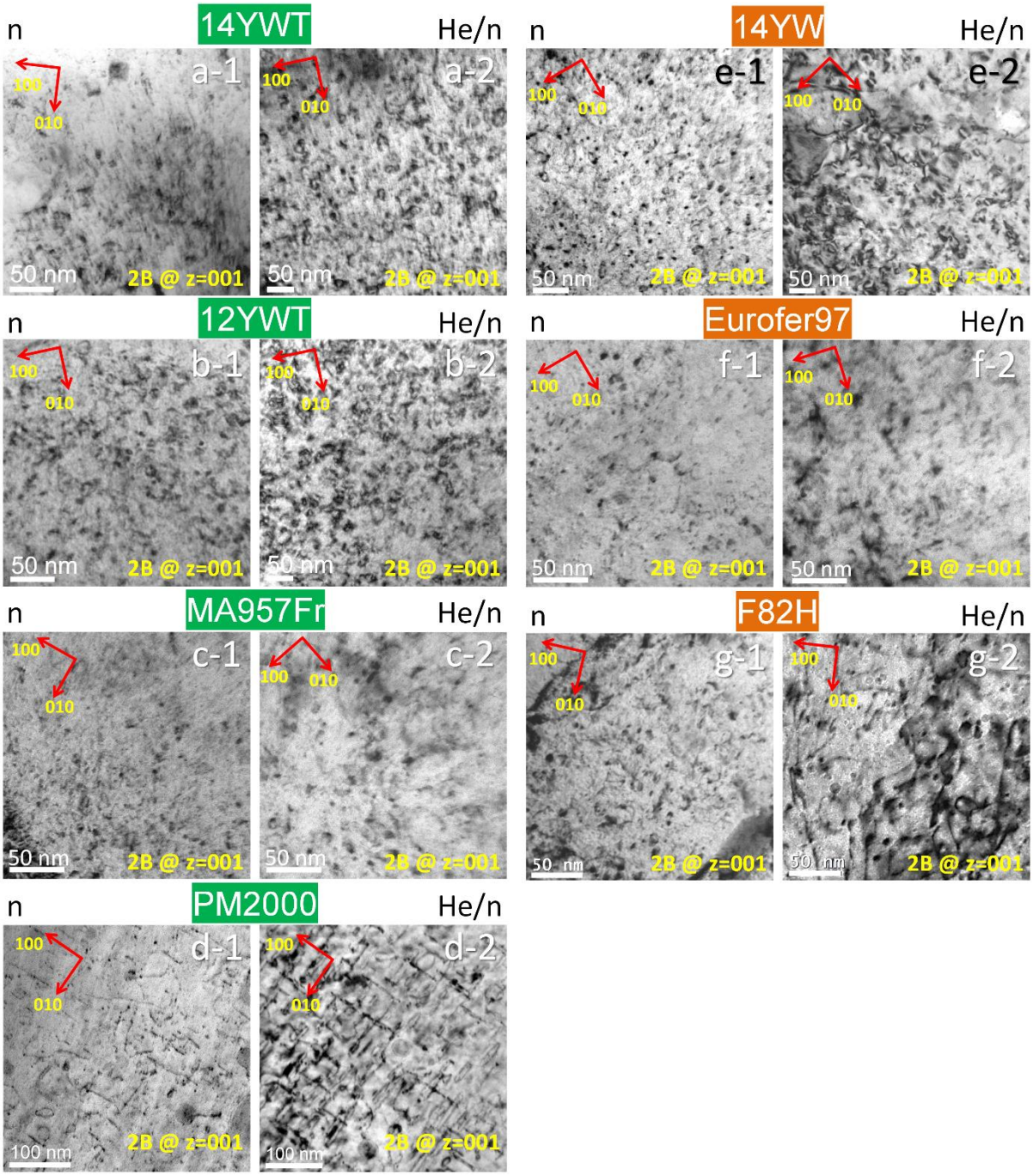

Figure 1. Examples are shown of the dislocation loop microstructure and the network dislocations that form in the irradiated samples. The images provide a comparison of both sides of the TEM disc, that is, with and without helium injection. PM2000 is the only alloy that shows a high density of large, arrayed loops.

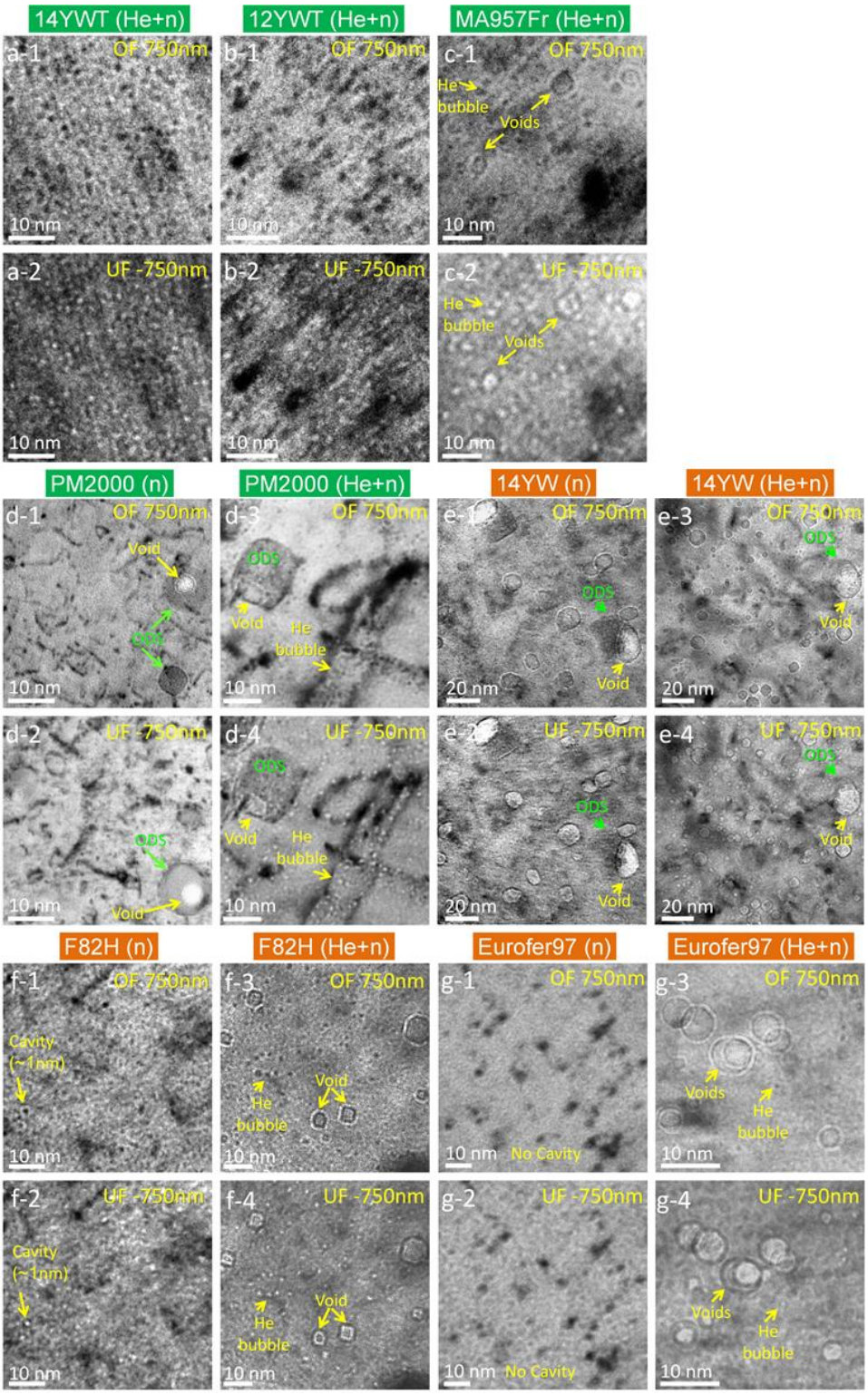

Figure 2. Helium bubbles and void microstructures are shown for each of the irradiated alloys and conditions in this study. Examples are provided for the helium-injected side along with a comparison of the non-injected side of the foil.

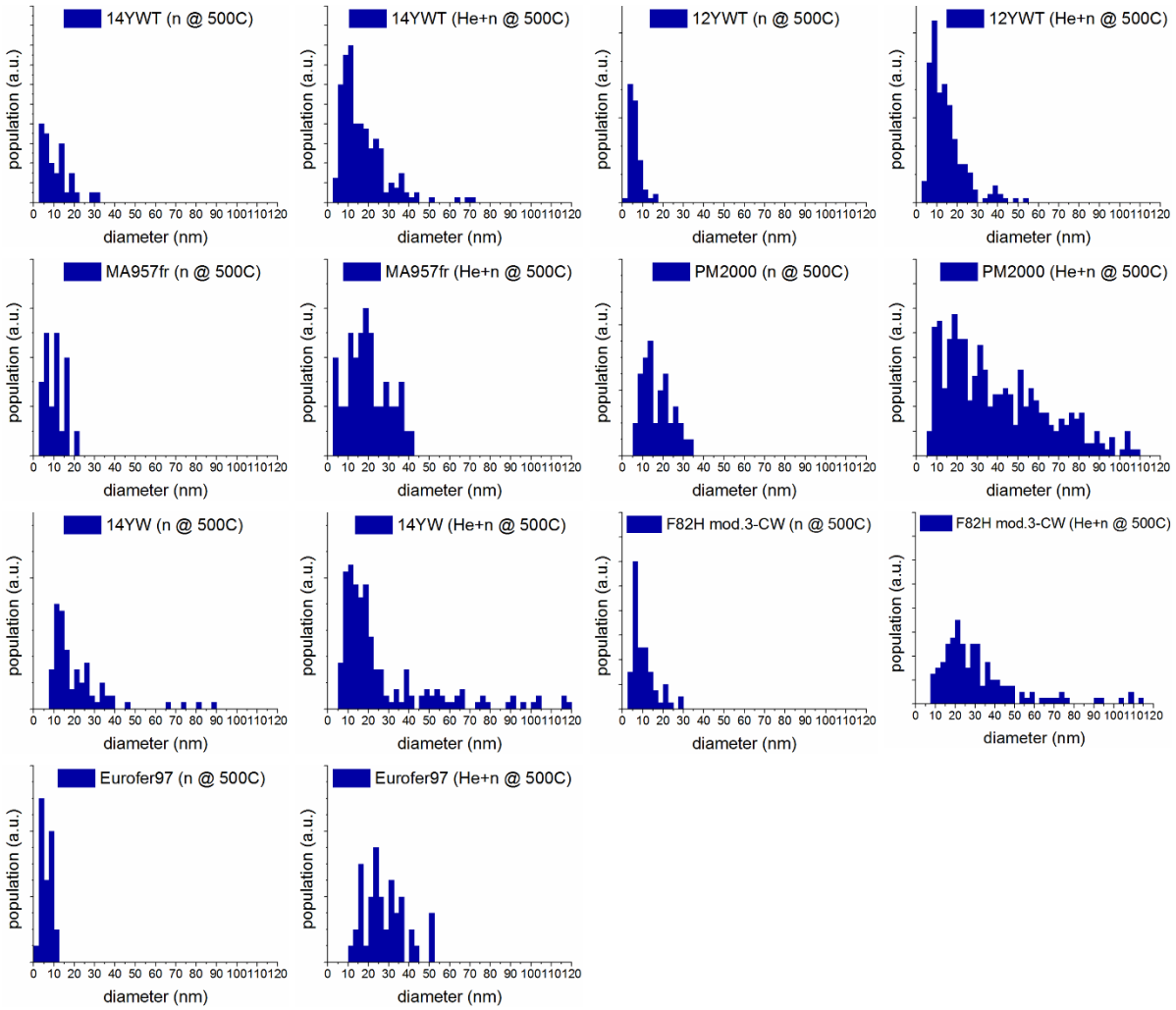

Figure 3. Histograms of <100>/{100} loop size in ODS ferritic alloys (14YWT, 12YWT, MA957Fr, PM2000, 14YW) and RAFM steels (F82H mod.3-CW, Eurofer97) under only neutron-irradiation (left) and He/neutron-irradiation (right) at 500°C.

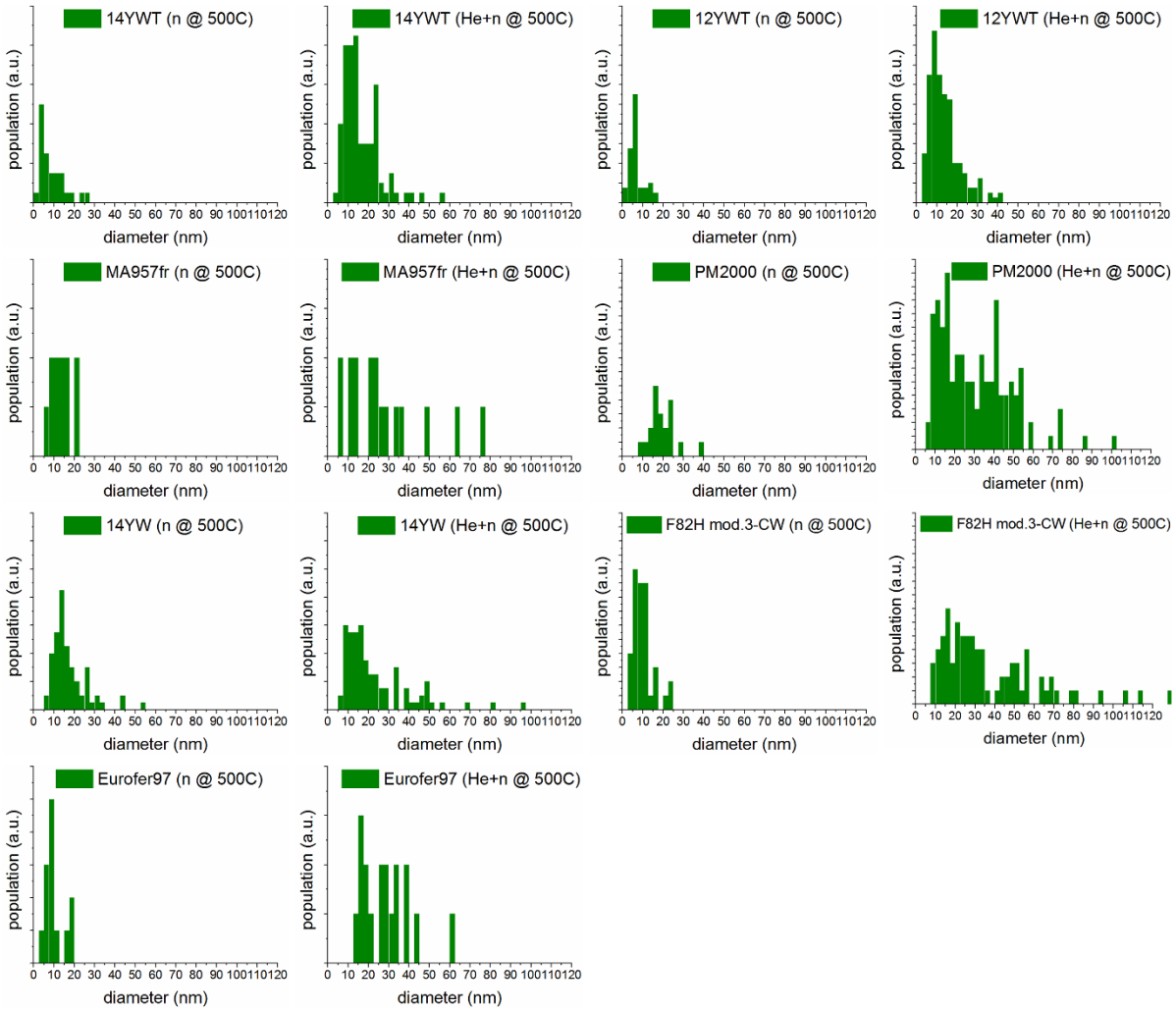

Figure 4. Histograms of 1/2<111>/{111} loop size in ferritic alloys (14YWT, 12YWT, MA957Fr, PM2000, 14YW) and RAFM steels (F82H mod.3-CW, Eurofer97) under only neutron-irradiation (left) and He/neutron-irradiation (right) at 500°C.

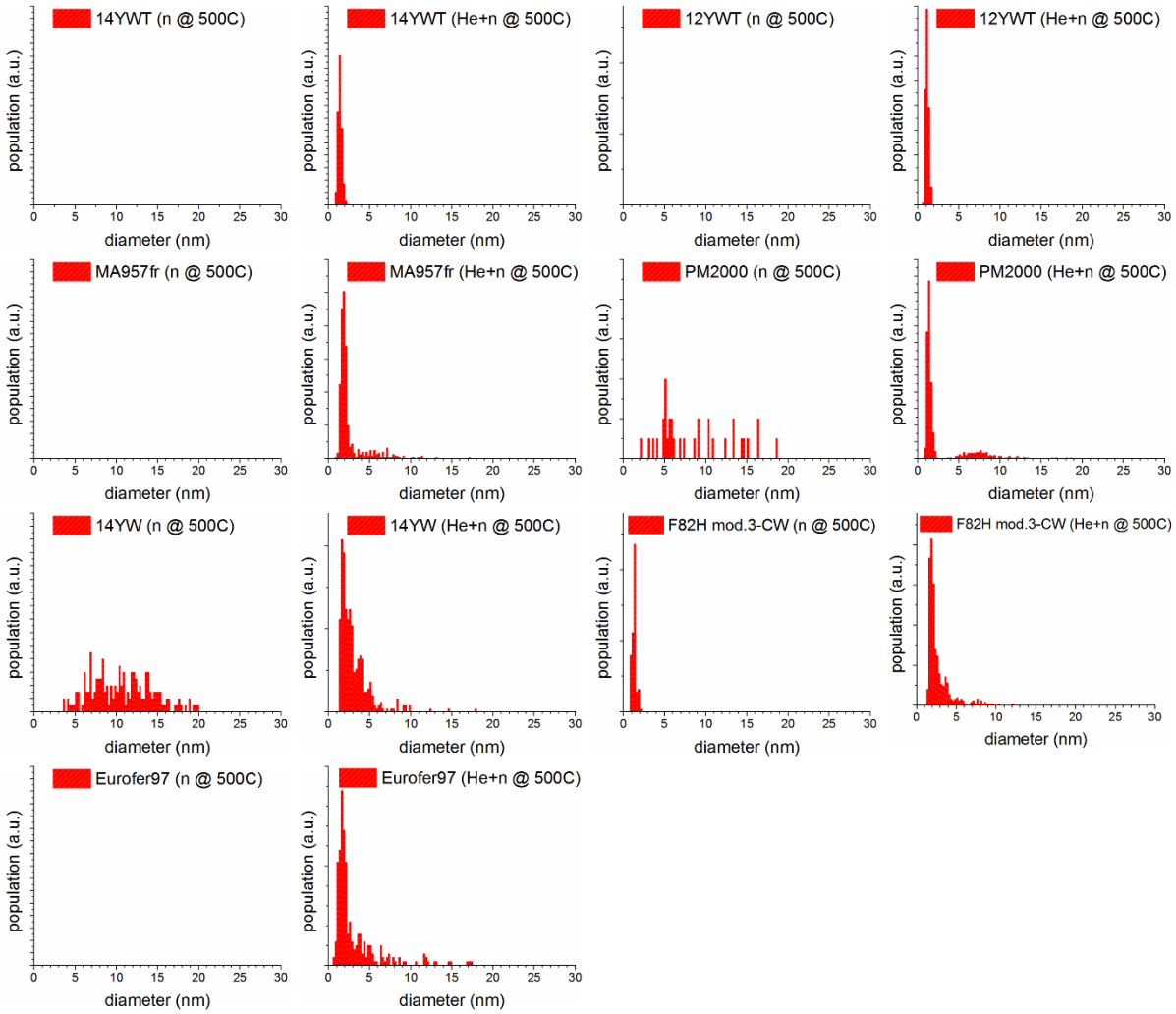

Figure 5. Histograms of bubble and voids in ferritic alloys 14YWT, 12YWT, MA957Fr, PM2000, 14YW and RAFM steels (F82H mod.3-CW, Eurofer97) under only neutron-irradiation (left) and He/neutron-irradiation (right) at 500 °C.

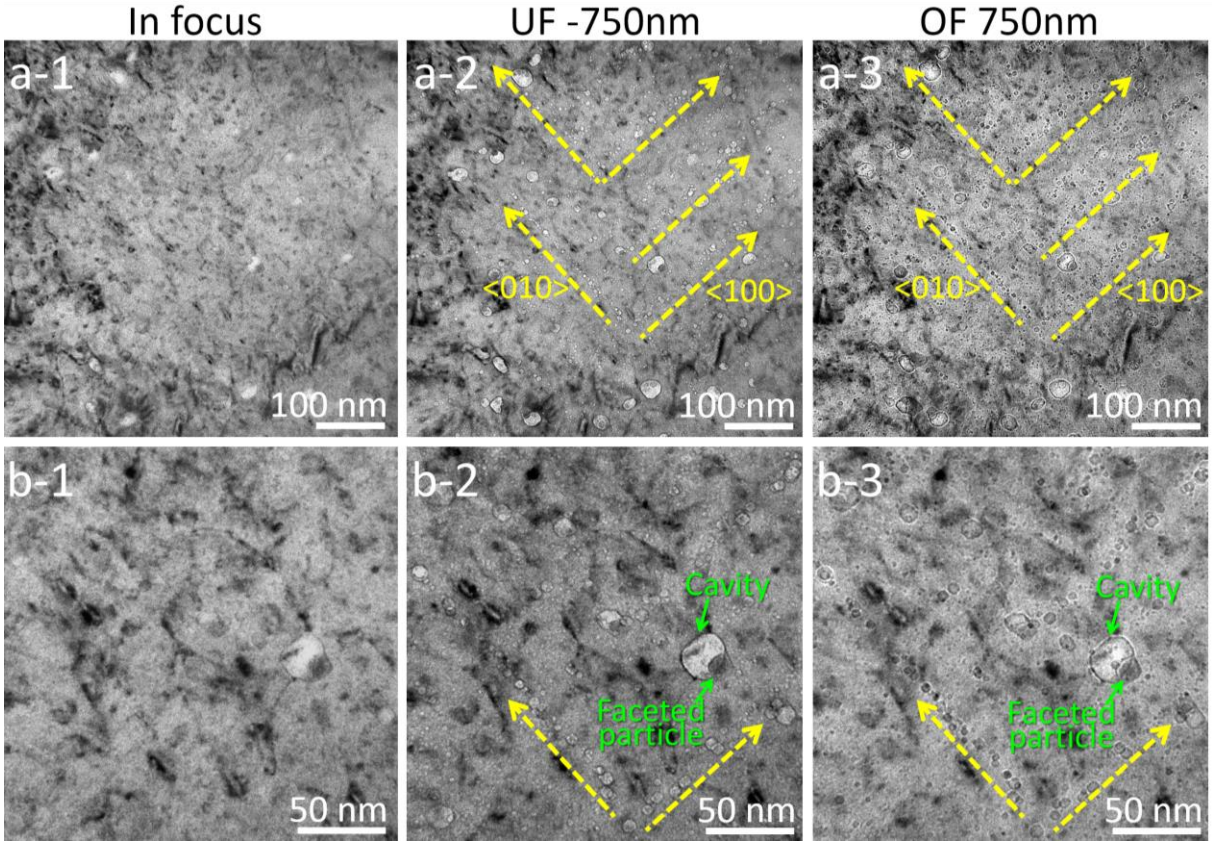

Figure 6. Two sets of through-focus BFTEM images taken near an [001] zone axis in the He-injected side of alloy 14YW show (a) He bubbles and cavities aligned to <100> directions (along yellow arrow), (b) large cavities (green) attached to rounded rectangular particle surface.

Acknowledgements

This research was supported by the U. S. Department of Energy, Office of Fusion Energy Sciences, under contract DE-AC06-76RLO1830 and DE-FG03-94ER54275. A portion of the research was performed using EMSL, a national scientific user facility sponsored by the DOE's Office of Biological and Environmental Research and located at PNNL.

References

[1] G.R. Odette, M.J. Alinger, B.D. Wirth, Annu. Rev. Mater. Res. 38 (2008) 471.
[2] R.J. Kurtz, A. Alamo, E. Lucon, Q. Huang, S. Jitsukawa, A. Kimura, R.L. Klueh, G.R. Odette, C. Petersen, M.A. Sokolov, P. Spätig, J.W. Rensman, J. Nucl. Mater. 386-388 (2009) 411.
[3] N. Baluc, K. Abe, J.L. Boutard, V.M. Chernov, E. Diegele, S. Jitsukawa, A. Kimura, R.L. Klueh, A. Kohyama, R.J. Kurtz, R. Lässer, H. Matsui, A. MÖslang, T. Muroga, G.R. Odette, M.Q. Tran, B. van der Schaaf, Y. Wu, J. Yu, and S.J. Zinkle, Nucl. Fusion 47 (2007) S696.
[4] R.E. Stoller, G.R. Odette, J. Nucl. Mater. 131 (1985) 118.
[5] T. Yamamoto, G.R. Odette, L.R. Greenwood, Fusion Materials Semiannual Progress Report for Period Ending June 30, 2005, DOE/ER-313/38 (2005) 95.

[6] T. Yamamoto, G.R. Odette, P. Miao, et al. J. Nucl. Mater. 367 (2007) 399.
[7] R.J. Kurtz, G.R. Odette, T. Yamamoto, D.S. Gelles, P. Miao, B.M. Oliver, J. Nucl. Mater. 367-370 (2007) 417.
[8] T. Yamamoto, G.R. Odette, P. Miao, J. Nucl. Mater. 386-388 (2009) 338.
[9] G.R. Odette, P. Miao, D.J. Edwards, T. Yamamoto, R.J. Kurtz, H. Tanigawa, J. Nuc. Mater. 417 (2011) 1001.
[10] B. Yao, D.J. Edwards, and R.J. Kurtz, J. Nucl. Mater. 434 (2012) 402.
[11] B. Yao, D.J. Edwards, R.J. Kurtz, G. R. Odette, T. Yamamoto, Fusion Materials Semiannual Progress Report for the Period Ending December 31, 2011, DOE-ER-0313/51 (2011) 85.
[12] B. Yao, D.J. Edwards, R.J. Kurtz, G.R. Odette, and T. Yamamoto, J. Electron Micros. 61(6) (2012) 393.
[13] H.J. Jung, D.J. Edwards, B. Yao, R.J. Kurtz, G.R. Odette, T. Yamamoto, Y. Wu, Fusion Materials Semiannual Progress Report for the Period Ending June 30, 2014, DOE-ER-0313/56 (2014) 19.